Split Active Asteroid P/2016 J1 (PANSTARRS)

Man-To Hui (許文韜)[1], David Jewitt[1,2], and Xinnan Du (杜辛楠)[2]
[1] Department of Earth, Planetary, and Space Sciences, UCLA, 595 Charles Young Drive East,
Box 951567, Los Angeles, CA 90095-1567, USA; pachacoti@ucla.edu
[2] Department of Physics and Astronomy, UCLA, 430 Portola Plaza, Box 951547, Los Angeles, CA 90095-1547, USA

Abstract

We present a photometric and astrometric study of the split active asteroid P/2016 J1 (PANSTARRS). The two components (hereafter J1-A and J1-B) separated either $\sim$1500 days (2012 May to June) or 2300 days (2010 April) prior to the current epoch, with a separation speed $V_{\text{sep}} = 0.70 \pm 0.02$ m s^{-1} for the former scenario and 0.83 ± 0.06 m s^{-1} for the latter. Keck photometry reveals that the two fragments have similar, Sun-like colors that are comparable to the colors of primitive C- and G-type asteroids. With a nominal comet-like albedo, $p_R = 0.04$, the effective, dust-contaminated cross sections are estimated to be 2.4 km^2 for J1-A and 0.5 km^2 for J1-B. We estimate that the nucleus radii lie in the range $140 \lesssim R_N \lesssim 900$ m for J1-A and $40 \lesssim R_N \lesssim 400$ m for J1-B. A syndyne–synchrone simulation shows that both components have been active for 3–6 months, by ejecting dust grains at speeds $\sim$0.5 m s^{-1} with rates $\sim$1 kg s^{-1} for J1-A and 0.1 kg s^{-1} for J1-B. In its present orbit, the rotational spin-up and devolatilization times of 2016 J1 are very small compared to the age of the solar system, raising the question of why this object still exists. We suggest that ice that was formerly buried within this asteroid became exposed at the surface, perhaps via a small impact, and that sublimation torques then rapidly drove it to breakup. Further disintegration events are anticipated owing to the rotational instability.

Key words: methods: data analysis – minor planets, asteroids: general –
minor planets, asteroids: individual (P/2016 J1)

1. Introduction

Active asteroids are solar system bodies that are dynamically asteroidal (Tisserand parameter with respect to Jupiter $T_J \gtrsim 3$) but have been observed to show comet-like mass-loss activity. To date, over 20 such objects have been discovered. Remarkably there is a broad range of different physical mechanisms that account for this activity, including rotational instability, sublimation of volatiles, impacts, and thermal fracture (Jewitt et al. 2015a).

P/2016 J1 (PANSTARRS; hereafter "2016 J1") was discovered on UT 2016 May 5 by the Panoramic Survey Telescope and Rapid Response System (PANSTARRS). Besides its asteroidal orbit and cometary appearance, it was observed to be split into two pieces, the brighter one designated as component J1-A and the fainter as component J1-B by the Minor Planet Center (MPC; Wainscoat et al. 2016). Previous unambiguous discoveries of split active asteroids include P/2013 R3 (Catalina-PANSTARRS with at least 10 components; Jewitt et al. 2014a) and 331P/2012 F5 (Gibbs with at least five components; Drahus et al. 2015). Therefore, 2016 J1 is the third member of this type. The two components are moving in nearly identical orbits (semimajor axis $a = 3.172$ au, eccentricity $e = 0.23$, and inclination $i = 14°.3$) and have an indistinguishable $T_J = 3.11$.

In this paper, we analyze Keck 10 m telescope images of 2016 J1 obtained on UT 2016 August 4 for physical properties of the two components (Sections 3 and 4), and we study the fragmentation dynamics based on new and published astrometric data (Section 5).

2. Observations

We obtained a sequence of images in the broadband B, V, and R filters on UT 2016 August 4, using the Keck I 10 m telescope on Mauna Kea, Hawaii. At this time, 2016 J1 was at heliocentric distance $r_H = 2.458$ au and geocentric distance $\Delta = 2.065$ au and had phase angle $\alpha = 23°.9$. The B-band observations, along with the V- and R-band observations, were performed simultaneously through the Low Resolution Imaging Spectrograph, which has independent blue and red channels separated by a dichroic beam splitter (Oke et al. 1995). We used the "460" dichroic, which has 50% transmission at 4875 Å. On the blue channel, we used a B-band filter with effective wavelength $\lambda_{\text{eff}} = 4370$ Å and FWHM of $\Delta \lambda = 878$ Å. On the red side, we took V- and R-band images. The V-band filter has $\lambda_{\text{eff}} = 5473$ Å and FWHM $\Delta \lambda = 948$ Å, and the R filter has $\lambda_{\text{eff}} = 6417$ Å and FWHM $\Delta \lambda = 1185$ Å.[3] Image exposure times were 250 s for the B-band data and 200 s for both the V- and R-band data. All images were taken with the telescope tracked non-sidereally to follow the apparent motion of 2016 J1 (30$''$ hr^{-1} in R.A., $-13''$ hr^{-1} in decl., approximately). The data were flat-fielded using images of a diffusely illuminated patch on the inside of the Keck dome, and photometric calibration was obtained from images of star PG 1633+099A from the Landolt catalog (Landolt 1992). The image scale of both channels is 0$''$.135 pixel^{-1}, while the seeing varied between $\sim$0$''$.6 and 0$''$.9 FWHM.

3. Photometric Results

We used synthetic circular apertures to extract photometry from the aligned, co-added images of 2016 J1. Our photometric aperture is 2$''$.0 in radius. Sky values were obtained from a contiguous annulus of 2$''$.0 in width centered at the target. Photometric uncertainties on 2016 J1, denoted as $\sigma_{m,\lambda}$, were estimated from error propagation, i.e., $\sigma_{m,\lambda} = \sqrt{\sigma_{*,s}^2 + \sigma_{*,\lambda}^2 + \sigma_I^2}$, where $\sigma_{*,s}$ is the standard deviation on

---

[3] https://www2.keck.hawaii.edu/inst/lris/filters.html

the mean of repeated measurements of PG 1633+099A, $\sigma_{*,\lambda}$ is the magnitude error of the star in the corresponding bandpass given by Landolt (1992), and σ_I is the uncertainty in instrumental magnitudes of the two components calculated from the gain and read noise of the instrument.

For convenience we denote the apparent magnitudes of components of 2016 J1 as $m_{\lambda,j}$, where λ refers to the bandpasses (B, V, or R) and j = a and b labels J1-A and J1-B, respectively. Our measurements yield $m_{a,B} = 23.04 \pm 0.03$, $m_{a,V} = 22.30 \pm 0.03$, and $m_{a,R} = 21.94 \pm 0.03$ for J1-A and $m_{b,B} = 24.78 \pm 0.08$, $m_{b,V} = 24.04 \pm 0.09$, and $m_{b,R} = 23.65 \pm 0.08$ for J1-B. Thus, we can find that two fragments have colors nearly identical to each other within the noise level: $(m_B - m_V)_a = 0.74 \pm 0.04$ and $(m_V - m_R)_a = 0.36 \pm 0.04$ for J1-A and $(m_B - m_V)_b = 0.74 \pm 0.12$ and $(m_V - m_R)_b = 0.39 \pm 0.12$ for J1-B, in comparison with the color indices of the Sun, $(m_B - m_V)_\odot = 0.65 \pm 0.01$ and $(m_V - m_R)_\odot = 0.35 \pm 0.01$ (Ramírez et al. 2012). Given the uncertainties, the color of 2016 J1 is indistinguishable from colors of the C- and G-type asteroids (e.g., Dandy et al. 2002). The latter are believed to have undergone minimal thermal processing.

We then investigate the normalized reflectivity gradients $S'_j(\lambda_1, \lambda_2)$ of the two components (j = a, b), defined by Jewitt & Meech (1986) as

$$S'_j(\lambda_1, \lambda_2) = \left(\frac{2}{|\Delta\lambda_{1,2}|} \right) \frac{10^{0.4[\Delta m_{1,2}^{(j)} - \Delta m_{1,2}^{(\odot)}]} - 1}{10^{0.4[\Delta m_{1,2}^{(j)} - \Delta m_{1,2}^{(\odot)}]} + 1}, \qquad (1)$$

where $\Delta\lambda_{1,2}$ is the difference in the effective wavelengths of the BVR filter pairs, $\Delta m_{1,2}$ is the color index in the pair, and the superscript in parentheses indicates the corresponding object. For component J1-A, we obtain $S'_a(V, B) = (7.3 \pm 3.6)\%$ per 10^3 Å and $S'_a(V, R) = (0.7 \pm 3.9)\%$ per 10^3 Å. For component J1-B, we have $S'_b(V, B) = (7.5 \pm 10.0)\%$ per 10^3 Å and $S'_b(V, R) = (3.6 \pm 11.8)\%$ per 10^3 Å. By comparison, the optical continuum reflectivity gradients of the active comets analyzed by Jewitt & Meech (1986) vary from $(5 \pm 2)\%$ to $(18 \pm 2)\%$ per 10^3 Å. Therefore, it is likely that the color of 2016 J1 is among the bluest of the measured coma colors, but is similar to those of the active asteroids, e.g., 133P/Elst-Pizarro (Hsieh et al. 2004) and 259P/Garradd (Jewitt et al. 2009). We expect that the color is dominated by scattering from dust particles in the coma, rather than from the nucleus surface.[4] A possibility that the scattering properties of the nucleus surface significantly differ from those of the dust grains in the coma cannot be ruled out. However, the Keck data do not reveal any statistically significant spatial variations in color.

We calculate the effective cross sections from the photometry using

$$C = \frac{\pi r_H^2 \Delta^2}{p_\lambda r_\oplus^2 \phi(\alpha)} 10^{-0.4(m_\lambda - m_{\odot,\lambda})}. \qquad (2)$$

Here r_H and Δ are the heliocentric and geocentric distances, both in meters, $r_\oplus \approx 1.5 \times 10^{11}$ m is the mean Sun–Earth distance, p_λ is the geometric albedo, and $\phi(\alpha)$ is the phase function of the coma, which we approximate as the

empirical phase function of dust (Marcus 2007; Schleicher & Bair 2011; http://asteroid.lowell.edu/comet/dustphase.html) and normalize at $\alpha = 0°$. To avoid potential gas contamination in the comae of components J1-A and J1-B, we focus on R band only. With a nominal, comet-like albedo $p_R = 0.04$ (Lamy et al. 2004) for both components of 2016 J1, Equation (2) yields $C = 2.4$ km^2 for J1-A and 0.5 km^2 for J1-B. Uncertainties in C are dominated by the unmeasured geometric albedo, which could easily be 50% smaller or larger (see Lamy et al. 2004).

If we further assume that the total cross section within our photometric aperture (radius $\vartheta = 9.7 \times 10^{-6}$ rad) is produced in a steady state with some effective particle speed ($v \sim 1$ m s^{-1}; see Section 4), then the residence time in the aperture is $\vartheta\Delta/v$ and the required mass-loss rate is

$$\dot{M} \sim \frac{\rho_d C \bar{a} v}{\vartheta \Delta}, \qquad (3)$$

where $\rho_d \sim 10^3$ kg m^{-3} is the bulk density of the dust grains, v is their speed, and $\bar{a}$ is their average radius. Substituting $v = 1$ m s^{-1} and $\bar{a} = 10^{-3}$ m, we obtain $\dot{M} \sim 1$ kg s^{-1} for J1-A and ~ 0.1 kg s^{-1} for J1-B. For comparison, the mass-loss rates of J1-A and J1-B inferred by extrapolation of an empirical relationship between absolute magnitude and gas production rate (Jorda et al. 2008) are $\dot{M} \approx 1.1$ and 0.4 kg s^{-1}, respectively, in better agreement with the estimates from the photometry than we could reasonably expect.

The photometry can also be used to provide upper limits to the sizes of J1-A and J1-B, by assuming that the inferred cross sections, $C = 2.4$ km^2 for J1-A and 0.5 km^2 for J1-B, are equal to those of the underlying nuclei. The effective radii of equal-area circles are calculated from $R_N \leqslant \sqrt{C/\pi}$, giving $R_N \approx 0.9$ km and 0.4 km for J1-A and J1-B, respectively. These are strong upper limits to the true nucleus radii because of the contaminating effects of near-nucleus dust.

Crude lower limits to the nucleus radii of J1-A and J1-B can be placed by assuming that the activity is driven by the equilibrium sublimation of exposed ice. We solved the energy balance equation to calculate the specific sublimation rate of $f_s = 1.6 \times 10^{-5}$ kg m^{-2} s^{-1} at $r_H = 2.46$ au. To supply mass loss at the rate of ~ 1 kg s^{-1} would then require an exposed area of $\sim 6.3 \times 10^4$ m^2, corresponding to a circular surface patch roughly 140 m in radius, which we take as a lower limit to the nucleus radius of J1-A. The equivalent lower-limit radius of J1-B is ~ 40 m. These estimates are clearly very uncertain because we do not know whether the activity is driven by sublimation and, even if it is, we do not know whether the sublimation occurs in equilibrium.

In summary, the nucleus radii are weakly constrained by the observations to lie in the range $140 \lesssim R_N \lesssim 900$ m for J1-A and $40 \lesssim R_N \lesssim 400$ m for J1-B. The photometry suggests that J1-A is larger than J1-B because J1-A is brighter, but evidence from split comets indeed shows that brightness and nucleus size are often not well correlated, with small fragments being more active, per unit area, than their larger, parent bodies (Boehnhardt 2004, p. 301). As a result, we cannot be sure of the relative sizes of J1-A and J1-B.

4. Morphology

Components J1-A and J1-B present similar morphologies in our Keck images, although the latter appears much fainter

---

[4] The expectation is based on comparison of the FWHM of stars (see Section 2) and that of the two components (FWHM $\sim 1\farcs3$ for J1-A, and $\sim 1\farcs9$ for J1-B, respectively).
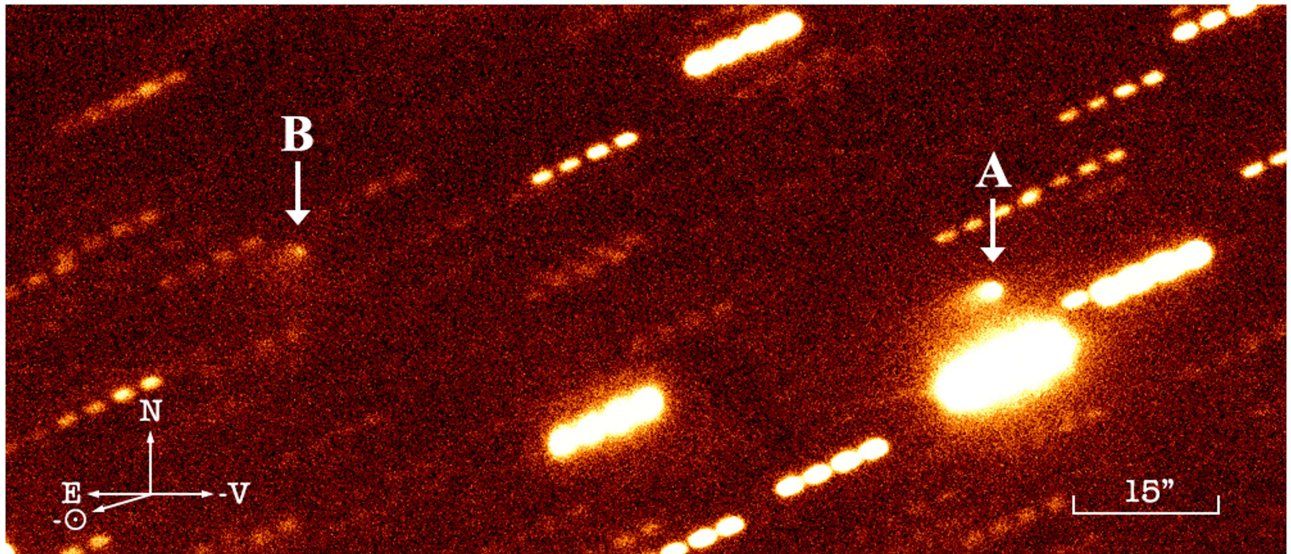
Figure 1. Keck I average image of components J1-A and J1-B (both arrowed and labeled) of active asteroid P/2016 J1 (PANSTARRS) on UT 2016 August 4 co-added from the individual *B*-, *V*-, and *R*-band images. As indicated by a compass in the lower left corner, equatorial north is up and east is left. The antisolar direction ($\theta_\odot$) and the negative heliocentric velocity vector projected on the sky plane (θ_V), respectively, are both shown. Also shown is a scale bar. The region shown is $\sim2'.2 \times 1'.0$. The dotted streaks are trails of background stars and galaxies.

(Figure 1). There is no evidence for a dust trail along the line of the projected orbit, as would be expected of very old, slow, presumably large particles ejected from either nucleus. To set a zeroth-order constraint on the dust properties implied by the morphology, we first adopt a method based on Finson & Probstein (1968) to calculate a syndyne–synchrone grid for 2016 J1. In this model, the dust grains are assumed to be released from the surface with zero initial velocity and are then progressively accelerated by solar radiation pressure. The particle trajectory is determined by the release time (τ) and the ratio between the solar radiation pressure force and the local gravitational force due to the Sun (β). A synchrone is the locus of positions of grains having varying β but with a common release time, and a syndyne is the line marking grains released at different times but subject to a common β.

The result is plotted in Figure 2. Although J1-B is very faint, we can still trace its fan-shaped tail, which is compatible with a series of syndynes having $\beta \lesssim 10^{-3}$ and $\tau \lesssim 200$ days. Interpreting J1-A quantitatively, however, is influenced by a nearby background star. Nevertheless, we are able to identify that the tail of J1-A is produced by $\beta \lesssim 2 \times 10^{-3}$ and $\tau \lesssim 100$ days. The grain size is related to the bulk density, ρ_d, and β by $\mathfrak{a} \propto (\rho_d \beta)^{-1}$, from which we can see that 2016 J1 has been releasing dust particles of at least submillimeter size, given an assumed density $\rho_d \sim 10^3 \, \mathrm{kg \, m^{-3}}$.

The syndyne–synchrone simulation alone does not provide any constraint on the ejection speeds of the dust grains, denoted as v_{ej}. The absence of a strong sunward extent to the coma, however, sets a rough limit to the ejection speed through the following equation:

$$v_{ej} \lesssim \frac{\sqrt{2\beta G M_\odot \Delta\ell}}{r_H},$$ (4)

where $G = 6.67 \times 10^{-11} \, \mathrm{N \, kg^2 \, m^2}$ is the gravitational constant, $M_\odot \approx 2 \times 10^{30}$ kg is the mass of the Sun, and ℓ is the apparent sunward turnaround distance expressed in radians. Our Keck images show $\ell \approx 1''.0$ for both components. By substitution with the corresponding values we obtain $v_{ej} \approx 2.4$
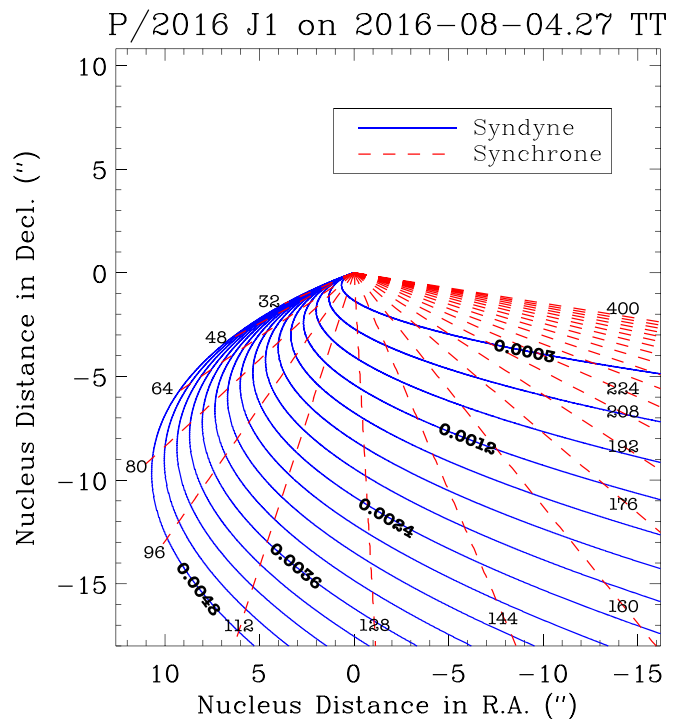

Figure 2. Syndyne–synchrone diagram for P/2016 J1 in comparison to Figure 1. Because of similarities of the orbits of two components, syndyne–synchrone differences are unnoticeable. As indicated, the blue lines are the syndynes, and the the dashed red lines are the synchrones. For clarity some of the syndynes and synchrones are labeled. The synchrone lines correspond to ejections from older days prior to the epoch from left to right, with the leftmost 16 days, rightmost 400 days, and an interval of 16 days. The syndyne lines have β decreasing anticlockwise, with the leftmost $\beta = 4.8 \times 10^{-3}$, rightmost 3×10^{-4}, and an interval of 3×10^{-4}.

and $1.7 \, \mathrm{m \, s^{-1}}$ from Equation (4) for submillimeter-sized dust grains of components J1-A and J1-B, respectively. The low ejection speed is similar to speeds measured in some other active asteroids, such as 133P/(7968) Elst-Pizarro (Jewitt et al. 2014b) and 313P/La Sagra (Jewitt et al. 2015b), in which little
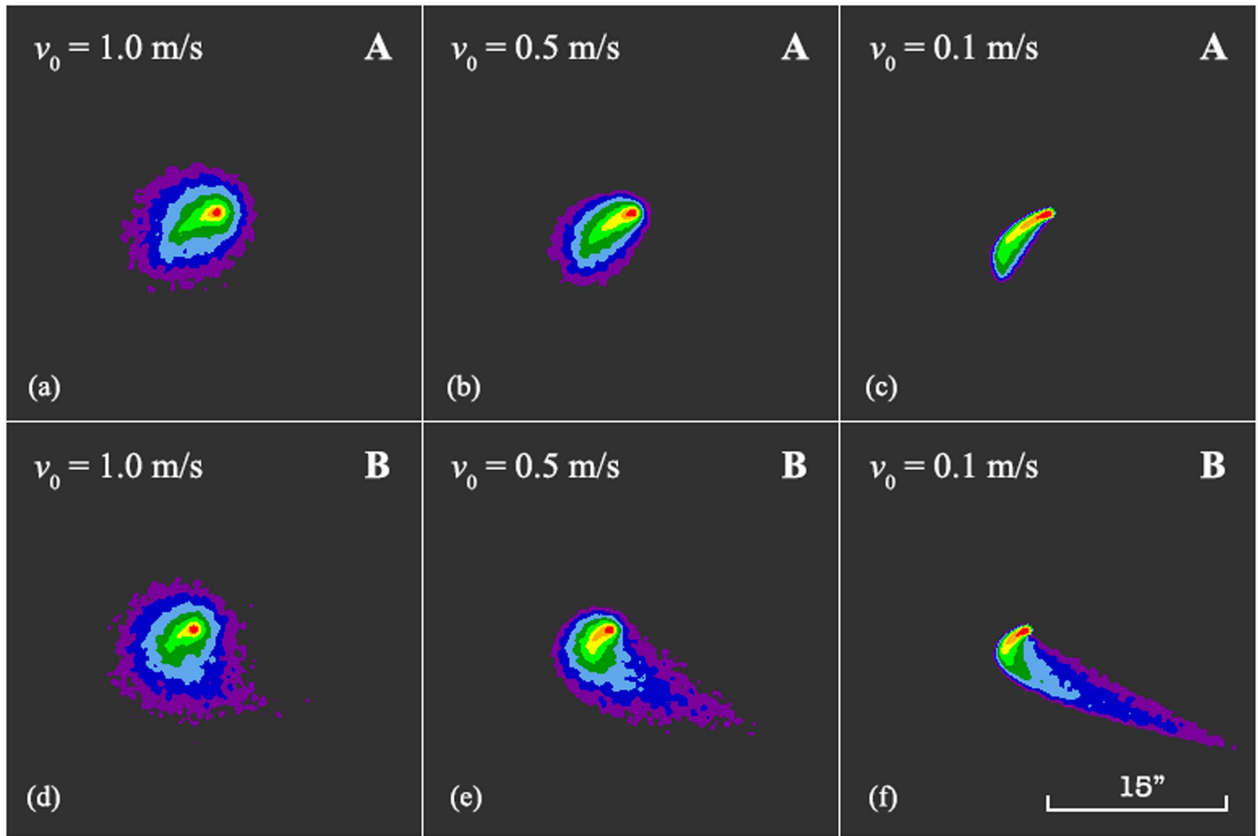
Figure 3. Modeled morphology of components J1-A (the first row, as indicated by the letter at the upper right corner of each panel) and J1-B (the second row) of active asteroid P/2016 J1 as a function of v_0. The values of v_0 are labeled explicitly for each panel. Other parameters remain fixed in the simulations for the same objects, i.e., the grain radius 0.3 mm $\leqslant \mathfrak{a} \leqslant$ 100 mm and the released time $\tau \leqslant$ 100 days for component J1-A and 0.6 mm $\leqslant \mathfrak{a} \leqslant$ 100 mm and $\tau \leqslant$ 200 days for component B. All the simulations have the differential slope index of the dust-size distribution $\gamma = 3.5$. A number of $\sim 10^4$ particles are generated in each run of the simulation. The modeled images are smoothed to mimic the seeing during the Keck observation. Also given is a scale bar, which is applicable to all the panels. Equatorial north is up, and east is left. By visual comparison, we conclude that the modeled images from the middle column best match the data.

or no sunward extent of the coma is observed. The likely cause is weak gas flow from a small source, or perhaps through a porous mantle.

We also considered a more realistic model where dust grains are emitted from the nucleus with nonzero initial velocities in a nucleus-centric frame, symmetric about the heliocentric radial direction facing toward the Sun, and satisfying a power-law size distribution. Similar to Ishiguro (2008), the ejection terminal speed is set to be correlated with the dust size and heliocentric distance, empirically expressed as

$$v_{\rm ej} = v_0 \sqrt{\frac{\mathfrak{a}_0 r_\oplus}{\mathfrak{a} r_{\rm H}}}, \qquad (5)$$

where v_0 is the ejection speed of dust particles of $\mathfrak{a}_0 = 0.5$ cm in radius at heliocentric distance $r_{\rm H} = 1$ au. The positions of generated dust grains at the observed time are then obtained by means of orbital integration in our modified version of the *mercury6* package (Chambers 1999), with inclusion of perturbations due to the eight major planets, Pluto, and the 10 most massive main-belt asteroids, although these perturbation effects are found to be minimal. Finally, we calculate a model image in which the intensity of each pixel is $\mathcal{I}(x, y)$,

$$\mathcal{I}(x, y) \propto \iint \left(\frac{\mathfrak{a}}{r_{\rm H}}\right)^2 \mathfrak{D}(x', y') dx' dy'. \qquad (6)$$

Here $\mathfrak{D}$ is the surface density of the dust particles in the sky plane as a function of pixel coordinates. In theory, a set of best-fit parameters can be solved such that the modeled image matches the observation the most closely. However, limitations of the data prevent us from obtaining meaningful results in the most general case. Instead, we vary only v_0 in Equation (5), while the differential power-law index γ remains fixed, because this is the parameter that will most affect the modeled morphology.

By trial and error, we determine that when $v_0 \sim 0.5$ m s^{-1}, the modeled and the observed morphologies match the best (Figure 3), a result that is true for both components. Larger speeds, e.g., $v_0 = 1$ m s^{-1}, create a tail that is too wide compared to the actual tail, while smaller speeds, e.g., $v_0 = 0.1$ m s^{-1}, result in tails that are too narrow. This conclusion is broadly consistent with our estimate of the ejection speed of submillimeter-sized dust grains as a few meters per second, provided that Equation (5) is valid. Other parameters do affect the morphology, but a detailed and exhaustive investigation is beyond the scope of this paper.

5. Split Dynamics

The similarities in the orbits of J1-A and J1-B of 2016 J1 (see Table 1) indicate a common origin. To investigate when the two components were produced, a straightforward method is to

Table 1
Orbital Solutions of Pair P/2016 J1-A and -B

Orbital Element	Component J1-A		Component J1-B	
	Value	1σ Uncertainty	Value	1σ Uncertainty
Semimajor axis a (au)	3.172092	1.83×10^{-5}	3.172014	2.18×10^{-5}
Perihelion distance q (au)	2.448015	1.25×10^{-5}	2.448063	1.57×10^{-5}
Eccentricity e	0.228265	3.45×10^{-6}	0.228231	5.42×10^{-6}
Inclination i (deg)	14.330194	9.59×10^{-5}	14.331156	1.35×10^{-4}
Longitude of ascending node Ω (deg)	199.856231	2.15×10^{-4}	199.855506	3.28×10^{-4}
Argument of perihelion ω (deg)	46.585537	4.50×10^{-3}	46.579240	6.68×10^{-3}
Time of perihelion t_P (TT)	2016 Jun 24.2138	1.49×10^{-2}	2016 Jun 24.1244	2.21×10^{-2}

Note. The orbital solutions were taken from the JPL Small-Body Database Browser. Osculating epochs for components J1-A and J1-B are TT 2016 Jun 20.0 and May 31.0, respectively. The normalized rms, which is defined as $\pm\sqrt{\sum_{i=1}^{N}\mathcal{R}_i^2 w_i^2/N}$, for component J1-A is ± 0.392 from 66 observations spanning UT 2016 March 04–August 04, and for J1-B it is ± 0.455 from 51 observations spanning UT 2016 March 17–August 04.

perform orbital integration backward for both components. However, we found that uncertainties in astrometric measurements have prevented us from obtaining a good constraint on the split epoch, because this method at best yields a nonzero close encounter distance of $\sim 10^{-4}$ au between the two components, which is unrealistic. We therefore created clones for each of the components based on the covariance matrices of the orbital elements and performed orbital integration for every clone. We then monitored their evolution in three-dimensional space visually in terms of orthogonal equatorial coordinates J2000 and observed that the two ellipsoids of clone clouds overlap with each other twice. The most recent period of overlap occurred ~ 1500–1800 days prior to the epoch of observation (roughly from 2011 November to 2012 April), and the earlier one occurred ~ 2500 days ago (2010 March to May).[5]

A potential nongravitational force will delay the best overlap epoch. Since the observing arc of 2016 J1 is too short, solving nongravitational parameters based on the astrometry only yields an unreliable result. Indeed, we have no detection. Besides, this method cannot provide good constraints on other parameters, such as the relative separation velocity of the secondary object. Dissatisfied, we exploited a different approach where we search for the best-fit fragmentation parameters, including the split epoch t_{frg}, the dimensionless radial nongravitational parameter of the secondary object $\tilde{\beta}$, which is mathematically the same as β but arises from anisotropic sublimation of volatiles, and the three Cartesian components of the separation velocity V_r, V_t, and V_n, in the radial, transverse, and normal directions instantly at t_{frg} centered at the primary object. A similar technique was developed by Sekanina (1978, 1982) and has been applied repeatedly (e.g., Meech et al. 1995; Sekanina & Chodas 2002). A major difference exists in terms of dealing with the nongravitational acceleration between the two models, in that the model by Sekanina (1978, 1982) solves for the differential deceleration of the secondary component with respect to the primary. In cases where the primary nucleus has no detectable nongravitational effects, the difference disappears.

At the splitting epoch t_{frg}, position coordinates of the primary nucleus and the fragment are the same, only with a difference in their velocities. Gravitational interactions between the components are ignored. We then integrate the

state vector of the secondary by the *mercury6* package in combination with planetary ephemeris DE431 and perturbations from the eight major planets, Pluto, and the 10 most massive main-belt asteroids all included. Topocentric positions of the secondary at each observed epoch are then compared to the observed position. We iterate the same procedure until the split parameters minimize the following quantity:

$$\chi^2(t_{frg}, \boldsymbol{V}_r, \boldsymbol{V}_t, \boldsymbol{V}_n, \tilde{\beta}) = \sum_{i=1}^{N}\mathcal{R}_i^2 w_i^2, \qquad (7)$$

where N is the total number of scalar astrometric observations, $\mathcal{R}_i^2$ is the squared astrometric residual in R.A. and decl., and w_i is the weight of the ith observation assigned based on the observation quality of components J1-A and J1-B.[6] Here, different astrometric observations are assumed to be uncorrelated with each other, which is usually a good approximation.

We first regarded J1-B as the principal nucleus of the active asteroid, because it is the leading component and was apparently located close to the negative heliocentric velocity vector projected onto the sky plane. In the process of finding the best-fit solution, we attempted various approaches. First, we searched for a solution mathematically equivalent to a syndyne–synchrone computation, where the total initial separation velocity V_{sep} was forced to be zero, while t_{frg} and $\tilde{\beta}$ were the two free parameters to be optimized, with an initial guess of t_{frg} in 2012. The solution did converge, but the result cannot be accepted, for it produced a strong systematic bias in the astrometric residuals considerably greater than the assigned uncertainties, along with a huge $\chi^2 > 2.1 \times 10^4$. Second, we included the three components of V_{sep} as free parameters to be solved, resulting in χ^2 declining appreciably and finally converging to $\chi^2 = 17.7$. However, this solution produced $\tilde{\beta} < 0$ with a signal-to-noise ratio (S/N) < 5. We regard this as likely bogus because a single run heavily relies on the orbit of J1-B, the quality of which is not optimum. To address this, we created 100 Monte Carlo (MC) clones of J1-B in accord with the covariance matrix of its orbital elements. For each of the clones, a set of best-fit split parameters were optimized. In this way we found a less significant $\tilde{\beta}$ (S/N = 3.3).

---

[5] This part of the work was done using the *SOLEX* package by A. Vitagliano.

[6] The task was accomplished by exploiting *MPFIT* (Markwardt 2009).

Table 2
Fragmentation Solutions for Pair P/2016 J1-A and -B

Quantity	Solution I		Solution II	
	Single Run	MC Iteration[a]	Single Run	MC Iteration
Split epoch $t_{\rm frg}$ (TT)	2012 May 18.6 ± 14.8	2012 May 19.5 ± 8.1	2010 Apr 11.8 ± 8.3	2010 Apr 08.7 ± 3.5
Separation velocity (m s^{-1}):				
Radial component $\mathbf{V_r}$	−0.6450 ± 0.0169	−0.6458 ± 0.0079	+0.7486 ± 0.0597	+0.7556 ± 0.0258
Transverse component $\mathbf{V_t}$	+0.0295 ± 0.0063	+0.0296 ± 0.0029	−0.0327 ± 0.0089	−0.0309 ± 0.0035
Normal component $\mathbf{V_n}$	−0.2798 ± 0.0089	−0.2803 ± 0.0040	+0.3624 ± 0.0180	+0.3553 ± 0.0064
Weighted rms[b] ($''$)	±0.123	∈ ± [0.105, 0.154]	±0.101	∈ ± [0.099, 0.126]
Normalized rms	±0.569	∈ ± [0.483, 0.713]	±0.465	∈ ± [0.459, 0.580]

Notes. Both methods completely selected the same astrometric data and adopted the same weighting scheme as those used to solve an orbit for component J1-B in Table 1. The dimensionless nongravitational parameter $\tilde{\beta}$ is forced to be zero in all of the runs.
[a] One hundred clones of synthesized J1-A are created based on the covariance matrix of its orbital elements. The uncertainties are standard deviations on the mean values.
[b] The weighted rms is calculated from $\pm\sqrt{\sum_{i=1}^{N}\mathcal{R}_i^2 w_i^2/\sum_{i=1}^{N}w_i^2}$. For the MC iterations, the minimum and the maximum of the unsigned weighted rms are given.

We then forced $\tilde{\beta} \equiv 0$ exactly and exploited the routine to search for four other free parameters ($t_{\rm frg}$ and the three Cartesian components of $V_{\rm sep}$). Although the converged solution yielded a larger $\chi^2 = 35.0$, we did not notice any systematic bias beyond or comparable to the uncertainty levels. The same procedures were attempted for finding a solution with an initial guess of $t_{\rm frg}$ in 2010. Our routine yielded an equally good solution (e.g., $\chi^2 = 17.7$ for all the five splitting parameters regarded as free parameters producing $\tilde{\beta} < 0$, and $\chi^2 = 22.2$ for the scenario of $\tilde{\beta} \equiv 0$). We therefore conclude that there is no compelling evidence for the existence of nongravitational effects on component J1-A, consistent with the aforementioned fact that the ordinary orbit determination revealed no statistically significant nongravitational parameters. Instead, the relative positions of J1-A and J1-B are overwhelmingly determined by the separation velocity of the two fragments, rather than by any differential nongravitational force. For this reason, we cannot use dynamics to ambiguously determine which component is the principal nucleus of 2016 J1.

We then took advantage of the fact that the orbital solution of J1-A has a better quality and solved the splitting parameters by regarding J1-A as the primary. Again there is no reliable detection of $\tilde{\beta}$ for component J1-B, and so we set $\tilde{\beta} \equiv 0$. Table 2 summarizes the two equally good best-fit solutions for $t_{\rm frg}$ in 2012 and 2010, and we present the corresponding astrometric residuals in Table 3. We also created 100 MC clones of J1-A from its covariance matrix of the orbital elements and performed optimization repeatedly. The statistics are listed in Table 2, consistent with the results from the single runs. The split event occurred either at some point around 2012 May to June, when 2016 J1 was $r_{\rm H} \approx 3.4$–3.5 au from the Sun, with a total separation speed $V_{\rm sep} = 0.70 \pm 0.02 \, {\rm m \, s^{-1}}$, or in 2010 April, when it was $r_{\rm H} \approx 2.6$ au, with a total separation speed $V_{\rm sep} = 0.83 \pm 0.06 \, {\rm m \, s^{-1}}$, mainly in the radial direction. We have no strong basis for preferring one solution over the other. The separation speed value falls within the range of values shown by split Kuiper Belt and Oort cloud comets (see Sekanina 1982; Boehnhardt 2004, p. 301). Unfortunately, the physical mechanism leading to fragmentation of 2016 J1 cannot be constrained by dynamics, because different splitting mechanisms can lead to similar separation speeds.

5.1. Lifetime

For illustrative purposes in this section, we adopt a radius $R_{\rm N} \sim 300 \, {\rm m}$ for both components of 2016 J1; this value is consistent with the observational constraints described above. We evaluated the devolatilization timescale $\tau_{\rm dv}$ by

$$\tau_{\rm dv} \sim \frac{\rho_{\rm d} R_{\rm N}}{f_{\rm s}}, \qquad (8)$$

where $f_{\rm s}$ is the time-averaged equilibrium specific sublimation rate around the orbit. In its present orbit, 2016 J1 travels from $r_{\rm H} = 2.45$ au at perihelion to 3.89 au at aphelion. Over this range, we calculate $f_{\rm s} = 4.4 \times 10^{-6} \, {\rm kg \, m^{-2} \, s^{-1}}$. Substituting the values from Section 3, Equation (8) yields $\tau_{\rm dv} \sim 7 \times 10^{10} \, {\rm s}$, or $\sim$2 kyr as the approximate devolatilization timescale for 2016 J1. It is worth pointing out that this value is only a lower limit, because the growth of a refractory mantle is likely to impede outgassing as a result of an aging nucleus (Rickman et al. 1990).

A short lifetime is also indicated by simple models of rotational instability, driven by outgassing torques (Jewitt 1997; Jewitt et al. 2016). For example, Equation (3) of the latter paper gives an e-folding spin-up time $\tau_{\rm s} \sim 0.2 \, {\rm kyr}$, for an assumed period of 5 hr, radius 0.3 km, outgassing speed $\sim$0.5 km s^{-1}, dimensionless moment arm of the torque $k_{\rm T} = 10^{-3}$, and mass-loss rate $\dot{M} \sim 1 \, {\rm kg \, s^{-1}}$. The moment arm is unknown to within at least an order of magnitude ($0.0004 \leqslant k_{\rm T} \leqslant 0.04$; Gutiérrez et al. 2003; Belton et al. 2011; Drahus et al. 2011), so that this timescale, like $\tau_{\rm dv}$, is approximate. Nevertheless, it is evident that the components of 2016 J1 are likely to be short-lived.

Given that the sublimation and rotational spin-up timescales are small compared to the 4.5 Gyr age of the solar system, the question arises as to why 2016 J1 survives at all. The answer, as is the case for the main-belt comets generally, presumably lies with the long-term history and stability of the near-surface ice (e.g., Hsieh & Jewitt 2006). Conduction models show that near-surface ice can be stabilized against sublimation by a modest (meter-sized thick) refractory, particulate layer (Schorghofer 2008). Buried ice can persist in the asteroid belt with negligible sublimation losses for times comparable to the age of the solar system. Only when exposed at the surface, by a small impact or other disturbance, can the ice sublimate. We thus imagine that the long-term

Table 3
Astrometric Residuals in Best-fit Solutions for P/2016 J1-A and -B

Observation Time (UT)	Residuals I[a] (″)		Residuals II[b] (″)		Uncertainty (″)	Observatory Code[c]
	R.A.	Decl.	R.A.	Decl.		
2016 Mar 17.622098	+0.268	−0.269	+0.097	+0.052	0.30	568
2016 Apr 14.53944	+0.256	−0.582	+0.047	−0.392	0.70	F51
2016 Apr 14.55134	−0.488	+0.275	−0.697	+0.465	0.70	F51
2016 Apr 14.56324	−0.032	−0.773	−0.241	−0.584	0.70	F51
2016 Apr 14.57510	+0.262	−0.205	+0.053	−0.015	0.70	F51
2016 May 06.425891	+0.137	+0.029	+0.043	+0.085	0.20	568
2016 May 06.427167	+0.116	+0.037	+0.023	+0.093	0.20	568
2016 May 07.445034	+0.096	+0.075	+0.010	+0.125	0.20	568
2016 May 07.447008	+0.160	−0.040	+0.074	+0.010	0.20	568
2016 May 07.448979	+0.162	+0.017	+0.076	+0.067	0.20	568
2016 May 08.349285	−0.025	−0.003	−0.104	+0.042	0.50	H01
2016 May 08.360538	+0.057	−0.073	−0.022	−0.028	0.50	H01
2016 May 08.363089	+0.139	+0.083	+0.060	+0.128	0.50	H01
2016 May 08.368020	+0.197	−0.309	+0.118	−0.264	0.50	H01
2016 May 08.371138	+0.180	−0.375	+0.101	−0.330	0.50	H01
2016 May 11.465427	+0.087	+0.052	+0.030	+0.080	0.20	568
2016 May 11.466126	+0.088	−0.240	+0.031	−0.212	0.30	568
2016 May 11.469146	+0.161	−0.050	+0.105	−0.022	0.15	568
2016 May 11.471359	+0.044	−0.060	−0.013	−0.032	0.15	568
2016 May 15.092581	+0.061	−0.079	+0.030	−0.069	0.20	Z18
2016 May 15.094942	+0.045	−0.033	+0.014	−0.023	0.20	Z18
2016 May 15.097292	+0.157	−0.052	+0.126	−0.042	0.20	Z18
2016 May 15.099653	+0.201	−0.196	+0.169	−0.186	0.20	Z18
2016 May 15.102002	+0.116	−0.195	+0.085	−0.185	0.20	Z18
2016 May 29.044549	−0.070	+0.062	−0.015	+0.023	0.10	Z18
2016 May 29.046898	−0.092	+0.044	−0.037	+0.006	0.10	Z18
2016 May 29.049248	−0.084	+0.057	−0.029	+0.019	0.10	Z18
2016 May 29.051609	−0.114	+0.076	−0.060	+0.037	0.10	Z18
2016 May 29.053958	−0.123	+0.089	−0.068	+0.050	0.10	Z18
2016 Jun 06.339455	−0.026	−0.072	+0.063	−0.122	0.50	695
2016 Jun 07.314874	+0.100	−0.403	+0.193	−0.454	0.50	695
2016 Jun 09.279018	−0.405	−0.011	−0.307	−0.064	0.50	695
2016 Jun 11.281689	−0.242	−0.128	−0.139	−0.181	0.50	695
2016 Jun 12.185745	+0.170	−0.349	+0.275	−0.402	0.50	695
2016 Jul 31.944329	+0.351	−0.243	+0.372	−0.208	0.30	Z18
2016 Jul 31.946678	+0.224	−0.241	+0.245	−0.206	0.30	Z18
2016 Jul 31.949039	+0.149	+0.065	+0.169	+0.100	0.30	Z18
2016 Jul 31.953738	+0.146	−0.231	+0.166	−0.196	0.30	Z18
2016 Aug 04.269988	−0.024	−0.012	−0.015	+0.029	0.30	568
2016 Aug 04.270127	+0.041	+0.032	+0.050	+0.074	0.30	568
2016 Aug 04.274039	−0.211	+0.098	−0.202	+0.140	0.30	568
2016 Aug 04.274178	−0.236	−0.007	−0.227	+0.035	0.30	568
2016 Aug 04.278345	−0.178	+0.011	−0.169	+0.052	0.30	568
2016 Aug 04.278472	−0.120	+0.012	−0.111	+0.053	0.30	568
2016 Aug 04.282234	−0.071	−0.001	−0.062	+0.041	0.30	568
2016 Aug 04.282373	−0.156	+0.004	−0.148	+0.046	0.30	568
2016 Aug 04.287257	+0.072	+0.052	+0.080	+0.093	0.50	568
2016 Aug 04.287396	+0.391	−0.074	+0.400	−0.032	0.50	568
2016 Aug 04.292500	+0.323	−0.055	+0.332	−0.014	0.50	568
2016 Aug 04.297060	−0.404	+0.038	−0.396	+0.079	0.50	568
2016 Aug 04.297199	+0.155	−0.177	+0.164	−0.136	0.50	568

Notes.
[a] O–C residuals from the single-run best-fit solution I in Table 2.
[b] O–C residuals from the single-run best-fit solution II in Table 2.
[c] Corresponding names of the observatories and their geocentric coordinates are given by http://www.minorplanetcenter.net/iau/lists/ObsCodes.html.

survival of asteroid 2016 J1 reflects the past burial and recent excavation of its near-surface ice. In this scenario, a small, surface-disturbing impact can expose ice that produces a sublimation torque leading to breakup of the nucleus. Further splitting events are possible in the near future. We hence encourage follow-up observations of 2016 J1.

6. Summary

Key conclusions of our analysis of active asteroid P/2016 J1 (PANSTARRS) are summarized as follows.

1. The radii of the components are constrained to lie in the range $140 \lesssim R_N \lesssim 900$ m for J1-A and $40 \lesssim R_N \lesssim 400$ m for J1-B, assuming a comet-like geometric albedo $p_R = 0.04$.

2. The separation between J1-A and J1-B occurred either $\sim$1500 days (around 2012 May to June) or 2300 days (in 2010 April) before the present observations. The separation speed is $V_{sep} = 0.70 \pm 0.02 \,\mathrm{m\,s^{-1}}$ for the former case and $0.83 \pm 0.06 \,\mathrm{m\,s^{-1}}$ for the latter, mainly in the radial direction. A dust dynamics simulation shows that both components have been active (at rates up to $\sim$1 kg s^{-1}) for several months, but not for the full $\sim$1500 or 2300 days since breakup.

3. The component colors ($m_B - m_V = 0.74 \pm 0.04$ and $m_V - m_R = 0.36 \pm 0.04$ for J1-A and $m_B - m_V = 0.74 \pm 0.12$ and $m_V - m_R = 0.39 \pm 0.12$ for J1-B) are the same within the uncertainties. These nearly neutral colors are consistent with the spectra of primitive C- and G-type asteroids.

4. The sublimation and rotational spin-up lifetimes of J1-A and J1-B are much shorter than the 4.5 Gyr age of the solar system, implying that the observed activity cannot be sustained.

5. The breakup of 2016 J1 may itself be due to rotational instability induced by sublimation torques in an asteroid having recently exposed surface ice. We suggest that further disintegration events are possible in the near future, owing to continued rotational instability.

References

Bannister, M. T., Kavelaars, J. J., Petit, J.-M., et al. 2016, AJ, 152, 70
Belton, M. J. S., Meech, K. J., Chesley, S., et al. 2011, Icar, 213, 345
Boehnhardt, H. 2004, Comets II (Tucson, AZ: Univ. Arizona Press)
Chambers, J. E. 1999, MNRAS, 304, 793
Dandy, C. L., Fitzsimmons, A., Collander-Brown, S. J., Asher, D., & Bailey, M. E. 2002, in Asteroids, Comets, and Meteors, Optical colours of Near-Earth Objects, ed. B. Warmbein (Noordwijk: ESA), 915
Drahus, M., Jewitt, D., Guilbert-Lepoutre, A., et al. 2011, ApJL, 734, L4
Drahus, M., Waniak, W., Tendulkar, S., et al. 2015, ApJL, 802, L8
Finson, M. J., & Probstein, R. F. 1968, ApJ, 154, 327
Gutiérrez, P. J., Jorda, L., Ortiz, J. L., & Rodrigo, R. 2003, A&A, 406, 1123
Hsieh, H. H., & Jewitt, D. 2006, Sci, 312, 561
Hsieh, H. H., Jewitt, D. C., & Fernández, Y. R. 2004, AJ, 127, 2997
Ishiguro, M. 2008, Icar, 193, 96
Jewitt, D. 1997, EM&P, 79, 35
Jewitt, D., Agarwal, J., Li, J., et al. 2014a, ApJL, 784, L8
Jewitt, D., Hsieh, H., & Agarwal, J. 2015a, in Asteroids IV, ed. P. Michel, F. DeMeo, & W. Bottke (Tucson, AZ: Univ. Arizona Press), 221
Jewitt, D., Ishiguro, M., Weaver, H., et al. 2014b, AJ, 147, 117
Jewitt, D., Li, J., Agarwal, J., et al. 2015b, AJ, 150, 76
Jewitt, D., & Meech, K. J. 1986, ApJ, 310, 937
Jewitt, D., Mutchler, M., Weaver, H., et al. 2016, ApJL, 829, L8
Jewitt, D., Yang, B., & Haghighipour, N. 2009, AJ, 137, 4313
Jorda, L., Crovisier, J., & Green, D. W. E. 2008, in Asteroids, Comets, Meteors No. 1405, The Correlation Between Visual Magnitudes and Water Production Rates, 8046
Lamy, P. L., Toth, I., Fernandez, Y. R., & Weaver, H. A. 2004, in Comets II, ed. M. C. Festou, H. U. Keller, & H. A. Weaver (Tucson, AZ: Univ. Arizona Press), 223
Landolt, A. U. 1992, AJ, 104, 340
Marcus, J. N. 2007, ICQ, 29, 39
Markwardt, C. B. 2009, in ASP Conf. Ser. 411, Astronomical Data Analysis Software and Systems XVIII, ed. D. A. Bohlender, D. Durand, & P. Dowler (San Francisco, CA: ASP), 251
Meech, K. J., Knopp, G. P., Farnham, T. L., & Green, D. 1995, Icar, 116, 46
Oke, J. B., Cohen, J. G., Carr, M., et al. 1995, PASP, 107, 375
Ramírez, I., Michel, R., Sefako, R., et al. 2012, ApJ, 752, 5
Rickman, H., Fernandez, J. A., & Gustafson, B. A. S. 1990, A&A, 237, 524
Schleicher, D. G., & Bair, A. N. 2011, AJ, 141, 177
Schorghofer, N. 2008, ApJ, 682, 697
Sekanina, Z. 1978, Icar, 33, 173
Sekanina, Z. 1982, in Comets, ed. L. L. Wilkening (Tucson, AZ: Univ. Arizona Press), 251
Sekanina, Z., & Chodas, P. W. 2002, ApJ, 581, 760
Wainscoat, R. J., Woodworth, D., Micheli, M., et al. 2016, MPEC, 2016-J90